Monthly Notices
of the
ROYAL ASTRONOMICAL SOCIETY

MNRAS **487,** 168–180 (2019)
Advance Access publication 2019 April 27

doi:10.1093/mnras/stz1161

Cosmic ray transport and radiative processes in nuclei of starburst galaxies

Enrico Peretti [1,2]★ Pasquale Blasi [1,2] Felix Aharonian[1,3,4] and Giovanni Morlino[1,5]

[1]*Gran Sasso Science Institute, Viale F. Crispi 7, 67100, L'Aquila, Italy*
[2]*INFN/Laboratori Nazionali del Gran Sasso, via G. Acitelli 22, 67100, Assergi (AQ), Italy*
[3]*Max-Planck-Institute für Kernphysik, Saupfercheckweg 1, D-69117 Heidelberg, Germany*
[4]*Dublin Institute for Advanced Studies, 31 Fitzwilliam Place, D04 C932, Dublin 2, Ireland*
[5]*INAF/Osservatorio Astrofisico di Arcetri, L.go E. Fermi 5, 50125, Firenze, Italy*

Accepted 2019 April 22. Received 2019 March 5; in original form 2018 December 6

ABSTRACT

The high rate of star formation and supernova explosions of starburst galaxies make them interesting sources of high-energy radiation. Depending on the level of turbulence present in their interstellar medium, the bulk of cosmic rays produced inside starburst galaxies may lose most of their energy before escaping, thereby making these sources behave as calorimeters, at least up to some maximum energy. Contrary to previous studies, here we investigate in detail the conditions under which cosmic ray confinement may be effective for electrons and nuclei and we study the implications of cosmic ray confinement in terms of multifrequency emission from starburst nuclei and production of high-energy neutrinos. The general predictions are then specialized to three cases of active starbursts, namely, M82, NGC 253, and Arp220. Both primary and secondary electrons, as well as electron–positron pairs produced by gamma-ray absorption inside starburst galaxies are taken into account. Electrons and positrons produced as secondary products of hadronic interactions are found to be responsible for most of the emission of leptonic origin. In particular, synchrotron emission of very high energy secondary electrons produces an extended emission of hard X-rays that represents a very interesting signature of hadronic process in starburst galaxies, potentially accessible to current and future observations in the X-ray band. A careful understanding of both the production and absorption of gamma-rays in starburst galaxies is instrumental to the assessment of the role of these astrophysical sources as sources of high-energy astrophysical neutrinos.

Key words: cosmic rays – starburst.

1 INTRODUCTION

Starburst galaxies (SBGs) are unique sources showing a very intense star formation activity, at a level that can be as high as $\dot{M} \sim 10 \div 100\,\mathrm{M_\odot\,yr^{-1}}$, as discussed by Gao & Solomon (2004). Their star-forming regions, called starburst nuclei (SBNi), typically extend on few hundred parsec and are often observed in the cores of SGBs. The rapid star-forming activity, which reflects in an enhanced far-infrared (FIR) luminosity (Mannucci et al. 2003), leads to a correspondingly higher supernova rate, $\mathcal{R}_{SN} \sim 0.1 \div 1\ \mathrm{yr^{-1}}$, thereby suggesting that SBNi may be efficient sites of cosmic ray (CR) production.

The density of interstellar medium (ISM) in SBNi is estimated to be of the order of $n_{\rm ISM} \sim 10^2\,\mathrm{cm^{-3}}$, with a mass in the form of molecular clouds $M_{\rm mol} \sim 10^8\,\mathrm{M_\odot}$. The mass in the form of ionized gas is typically a few per cent of that of the neutral gas (a detailed discussion for the case of M82 was presented by Förster Schreiber et al. 2001). The FIR radiation can easily reach an energy density of $U_{\rm RAD} \sim 10^3\,\mathrm{eV\,cm^{-3}}$ while the strength of the inferred magnetic field is of order $B \sim 10^2 \div 10^3\,\mu\mathrm{G}$ (e.g. Thompson et al. 2006a). Moreover, the high supernova rate, together with a possible coexisting active galactic nucleus (AGN) activity, are expected to highly perturb the global SBN environment. Strong winds are in fact observed in many starbursts at every wavelength with estimated velocities of several hundred kilometre per second as reported for the case of M82 by Strickland & Heckman (2009), Engelbracht et al. (2006) and Seaquist & Odegard (1991).

Winds and turbulence play a fundamental role in CR transport in SBNi. The former lead to advection of CRs, a phenomenon that typically acts in the same way for CRs of any energy. The latter is responsible for CR diffusion through resonant scattering off perturbations in the magnetic field. The combination of wind advection, diffusion and energy losses shapes the transport of

★ E-mail: enrico.peretti@gssi.it

CRs in SBNi and determines whether or not the bulk of CRs is confined inside the nucleus, namely if particles lose most of their energy before escaping the nucleus (through either advection or diffusion). The phenomenon of CR confinement is crucial to understand the production of non-thermal radiation and neutrinos in SBGs. At energies where losses act faster than escape, the production of secondary electrons and positrons is prominent and in fact secondary electrons can be shown to be dominant upon primary electrons, for typical values of environmental parameters. In turn this implies that secondary electrons shape the multifrequency emission of SBNi through their synchrotron (SYN) and inverse Compton (IC) emission, a situation quite unlike the one of our Milky Way. Here, we study in detail under which conditions SBNi behave as calorimeters: We find that, for the conditions expected in SBNi, transport is dominated by advection with the wind up to very high energies. At sufficiently high energies (depending upon the level of turbulence), diffusion starts being dominant and leads to a transition to a regime where CR protons can leave the SBN before appreciable losses occur. In passing, we notice that the wind itself has been proposed as possible site where particle acceleration to extremely high energies might take place (Anchordoqui, Romero & Combi 1999; Anchordoqui 2018; Romero, Müller & Roth 2018).

Several models have been previously developed to describe the behaviour of CRs in starburst environments and infer their high-energy emission (Paglione et al. 1996; Torres 2004; Persic, Rephaeli & Arieli 2008; Rephaeli, Arieli & Persic 2010; Lacki & Thompson 2013). In all these works, diffusion effects were typically accounted for by assuming a diffusive escape time defined by a power-law energy dependence with slope $\delta = 0.5$ and a normalization of few millions of years at GeV energies. On the other hand, Yoast-Hull et al. (2013) assumed that CR transport is dominated solely by wind advection and energy losses, while diffusion would be negligible. Wang & Fields (2018) focused on hadronic gamma-ray emission in the framework in which SBNi are treated as calorimeters, whereas Sudoh, Totani & Kawanaka (2018) modelled the proton transport accounting for wind advection and Kolmogorov-like diffusion. SBGs have been also discussed as possible neutrino factories, both as isolated sources (Romero & Torres 2003; de Cea del Pozo, Torres & Rodriguez Marrero 2009; Yoast-Hull 2015) and as possible relevant contributors to the global diffuse flux (Loeb & Waxman 2006; Lacki et al. 2011; Tamborra, Ando & Murase 2014; Bechtol et al. 2017).

In this article, we improve with respect to previous studies in several respects: (1) the issue of calorimetric behaviour of SBNi is addressed in a quantitative way by discussing how different assumptions about the turbulence in the ISM of SBNi change the escape of CRs from the confinement volume as compared with the role of an advecting wind. This means that we can now also describe the transition from calorimetric behaviour to diffusion-dominated regime. This transition reflects into features in the spectrum of high-energy gamma-rays from the decay of neutral pions. (2) The spectrum of secondary electrons is self-consistently calculated taking into account advection, diffusion, and energy losses, so as to have at our disposal a self-consistent calculation of the multifrequency spectrum of radiation produced by electrons (primary and secondary) through SYN and IC scattering (ICS). (3) The absorption of gamma-rays as due to electron–positron pair production inside the starburst region is taken into account. This allows us to determine the spectrum of gamma-rays reaching us from an individual SBG and the contribution to the diffuse gamma-ray background. (4) The secondary electrons resulting from the decay of charged pions and from absorption of gamma-rays on the photon background inside an SBN both contribute to the production of a diffuse X-ray radiation as due to SYN emission. The detection of such emission would represent an unambiguous signature of the calorimetric behaviour of SBNi.

The paper is organized as follows: In Section 2, we describe the theoretical approach for the calculation of the CR distribution function inside a generic SBN and the associated photon and neutrino spectra. In Section 3, we discuss how different assumptions on the diffusion coefficient affect the confinement of cosmic rays inside SBNi and in Section 4 we apply our model to three SBGs, namely, NGC 253, M82, and Arp220 so as to have a calibration of our calculation to their observed multifrequency spectra. This allows us to have a physical understanding of CR transport in an SBG that can be applied to the determination of SBGs to the diffuse gamma and neutrino emission that will be discussed in detail in a forthcoming paper. We draw our conclusions in Section 5.

2 COSMIC RAY TRANSPORT IN AN SBN

Since the starburst nucleus of an SBG is rather compact and populated by both gas and sources, the simplest approach to CR transport in such a region is represented by a leaky-box-like model in which the injection of CR protons and electrons is balanced by energy losses, advection with a wind, and diffusion:

$$\frac{f(p)}{\tau_{\rm loss}(p)} + \frac{f(p)}{\tau_{\rm adv}(p)} + \frac{f(p)}{\tau_{\rm diff}(p)} = Q(p), \tag{1}$$

where f is the CR distribution function, Q is the injection term due to supernovae explosions, while $\tau_{\rm loss}$, $\tau_{\rm adv}$, and $\tau_{\rm diff}$ are the time-scales of energy losses, wind advection, and diffusion, respectively. The characteristic time for energy losses is derived combining effects due to radiative emission and collisions, namely

$$\frac{1}{\tau_{\rm loss}} = \sum_i \left(-\frac{1}{E}\frac{{\rm d}E}{{\rm d}t}\right)_i, \tag{2}$$

where i sums over ionization, proton–proton collisions and Coulomb interactions in the case of protons, whereas in the case of electrons it represents losses due to ionization, SYN, IC, and bremsstrahlung. The detailed expressions adopted for each channel are reported for completeness in Appendix A. The advection time-scale $\tau_{\rm adv}$ is the ratio between the SBN size and the wind speed, i.e. $\tau_{\rm adv} = R/v_{\rm wind}$, and provides an estimate of the typical time in which particles are advected away from the SBN. Similarly, the diffusion time-scale is taken as $\tau_{\rm diff}(p) = R^2/D(p)$, where $D(p)$ is the diffusion coefficient as a function of particle momentum. Here, we adopt an expression for $D(p)$ that is inspired by the quasi-linear formalism:

$$D(p) = \frac{r_L(p)v(p)}{3\mathcal{F}(k)}, \tag{3}$$

where $\mathcal{F}(k) = kW(k)$ is the normalized energy density per unit logarithmic wavenumber k, and $W(k) = W_0(k/k_0)^{-d}$, with $k_0^{-1} = L_0$ characteristic length-scale at which the turbulence is injected. We calculate $\mathcal{F}(k)$ by requiring the following normalization condition:

$$\int_{k_0}^{\infty} W(k){\rm d}k = \left(\frac{\delta B}{B}\right)^2 = \eta_B. \tag{4}$$

In order to bracket plausible models of CR diffusion in SBNi, we adopt three models of diffusion: (1) a benchmark model in which $d = 5/3$, $L_0 = 1$ pc, and $\eta_B = 1$ (model A), which leads to a Kolmogorov-like diffusion coefficient with asymptotic energy dependence $\sim E^{1/3}$; (2) a case in which $d = 0$ and $\eta_B = 1$ that leads to a Bohm diffusion coefficient (Model B); (3) a case in which $d =$

5/3 and η_B is normalized in such a way that the diffusion coefficient at 10 GeV is $\sim 3 \times 10^{28}$ cm^2 s^{-1}, which is supposed to mimic the diffusion coefficient inferred for our Galaxy (Model C). The latter case is expected to lead to faster diffusion and lesser confinement of CR protons in the SBN. In Model A, the choice of $L_0 \ll R$ was made to mimic an ISM with strong turbulence on pc scales. For the cases above, we choose a magnetic field $B = 200\,\mu$G and a size of the SBN $R = 200$ pc.

Given the starburst nature of the sources, it is expected that the main injection of CRs in SBNi occurs through supernova explosions. The injection term Q in equation (1) is assumed to be constant in the entire spherical volume and is computed as

$$Q(p) = \frac{\mathcal{R}_{\rm SN}\mathcal{N}_{\rm p}(p)}{V}, \tag{5}$$

where $\mathcal{N}_{\rm p}(p)$ is the injection spectrum of protons from an individual SNR, and $\mathcal{R}_{\rm SN}$ is the rate of SN explosions in the SBN volume V. Assuming that the spectrum of accelerated CR protons has the shape of a power law in momentum with index α up to a maximal value $p_{\rm max,p}$, we can write

$$\mathcal{N}_{\rm p}(p) \propto \left(\frac{p}{m_{\rm p}c}\right)^{-\alpha} e^{-p/p_{\rm p,max}}, \tag{6}$$

where the normalization constant is calculated by requiring that

$$\int_0^\infty 4\pi p^2 \mathcal{N}_{\rm p}(p) T(p) {\rm d}p = \xi_{\rm CR} E_{\rm SN}, \tag{7}$$

with $T(p)$ the kinetic energy of particles, $\xi_{\rm CR}$ the acceleration efficiency (of order 10 per cent), and $E_{\rm SN}$ the explosion energy for which we adopt the typical value of 10^{51} erg.

For electrons, the slope of the injection spectrum is assumed to be the same as for protons, but the cut-off is assumed to be as found in calculations of diffusive shock acceleration in the presence of energy losses and Bohm diffusion (Zirakashvili & Aharonian 2007; Blasi 2010):

$$\mathcal{N}_{\rm e}(p) \propto p^{-\alpha} e^{-(p/p_{\rm e,max})^2}. \tag{8}$$

Throughout the paper, we assume that $p_{\rm p,max} = 10^5$ TeV c^{-1} and $p_{\rm e,max} = 10$ TeV c^{-1}. We also assume that the spectrum of injected electrons has a lower normalization than protons by a factor $\sim$50, as also assumed by Torres (2004) and Yoast-Hull et al. (2013) and close to what is inferred for our Galaxy.

In order to quantify the confinement properties of SBNi, namely the situations in which CR protons and electrons lose energy before escaping the SBN, we adopt some reference values for the parameters, summarized in Table 1 and adopted in the estimates of time-scales for the different processes. We refer to this set of parameters as our '*reference case*'.

The time-scales for diffusion, advection, and energy losses for CR electrons and protons are shown in the top and bottom panels of Fig. 1, respectively. The horizontal (the dotted green) line refers to the advection time-scales, which is clearly independent of energy and is the same for electrons and protons. For typical values of the radius $R \sim 10^2$ pc (see e.g. Weaver et al. 2002) and wind velocity $v_{\rm wind} \sim 10^2 \div 10^3$ km s^{-1} (see e.g. Shopbell & Bland-Hawthorn 1998), the advection time-scale is of the order of a few hundred thousand years.

The time-scale for losses of electrons (the solid black line) shows an increasing trend for low momenta, reflecting the dominant ionization and bremsstrahlung channels. At high-energy SYN and IC scattering start being important and the loss time drops with energy approximately as E^{-1}. The time-scale for diffusive escape

Table 1. Table of parameters for the adopted reference case. $D_{\rm L}$ is the luminosity distance of the source, $\mathcal{R}_{\rm SN}$ is the supernova rate, R is the radius of the SBN, α is the injection index in momentum, B is the mean magnetic field and, $v_{\rm wind}$ is the outgoing wind velocity. The molecular cloud mass in the SBN is represented by $M_{\rm mol}$ and it coincides with an overall particle density given by $n_{\rm ISM}$. The ionized gas density is expressed by $n_{\rm ion}$ that has a temperature $T_{\rm plasma}$. The last four lines show the energy density U and the temperature kT of the three IR components due to dust and the optical one due to stars.

List of parameters	Value
$D_{\rm L}$ (Mpc) [redshift]	3.8 [8.8×10^{-4}]
$\mathcal{R}_{\rm SN}$ (yr^{-1})	0.05
R (pc)	200
α	4.25
B (μG)	200
$v_{\rm wind}$ (km s^{-1})	500
$M_{\rm mol}$ (10^8 M$_\odot$)	1.0
$n_{\rm ISM}$ (cm^{-3})	125
$n_{\rm ion}$ (cm^{-3})	18.75
$T_{\rm plasma}$(K)	6000
$U_{\rm Rad}^{\rm FIR}$ (eV cm^{-3}) [kT (meV)]	1101 [3.5]
$U_{\rm Rad}^{\rm MIR}$ (eV cm^{-3}) [kT (meV)]	330 [8.75]
$U_{\rm Rad}^{\rm NIR}$ (eV cm^{-3}) [kT (meV)]	330 [29.75]
$U_{\rm Rad}^{\rm OPT}$ (eV cm^{-3}) [kT (meV)]	1652 [332.5]

from the SBN for Model A (the dashed blue line), Model B (the dash–dotted red line), and Model C (the dash–dot–dotted magenta line) are also shown. For all these models, it is clear that energy losses dominate the transport of electrons at all energies. For Models A and B, the escape of electrons occurs due to wind advection, while for Model C there is a transition from advection to diffusion at energies $\sim$GeV. In any case, SNBi behave as electron calorimeters.

For CR protons, energy losses are dominated by ionization at low energies and by inelastic pp collisions at high energy. For the Models A and B of diffusive transport, the loss time-scales is always shorter than the time for diffusive escape. However, transport is dominated by wind advection at all energies of interest. The time-scale for advection and pp scattering remain comparable over many orders of magnitude in energy, due to the fact that both are roughly energy independent. In other words, SBNi behave as approximate, though not perfect, calorimeters. In Model C, CR transport is dominated by diffusion for energies above $\sim$GeV, and only a small fraction of the energy is lost during propagation. This latter case does not appear to be well motivated and is shown here only as a rather extreme scenario. Moreover, as we discuss next, the multifrequency spectra of individual SBGs are not easy to explain in the context of Model C.

2.1 Secondary and tertiary electrons and neutrinos

Electron–positron pairs are copiously produced in SBNi because of the severe rate of energy losses of CR protons. Following the approach put forward by Kelner, Aharonian & Bugayov (2006), we compute the pion injection rate as

$$q_\pi(E_\pi) = \frac{c n_{\rm ISM}}{K_\pi}\sigma_{\rm pp}\left(m_{\rm p}c^2 + \frac{E_\pi}{K_\pi}\right) n_{\rm p}\left(m_{\rm p}c^2 + \frac{E_\pi}{K_\pi}\right), \tag{9}$$

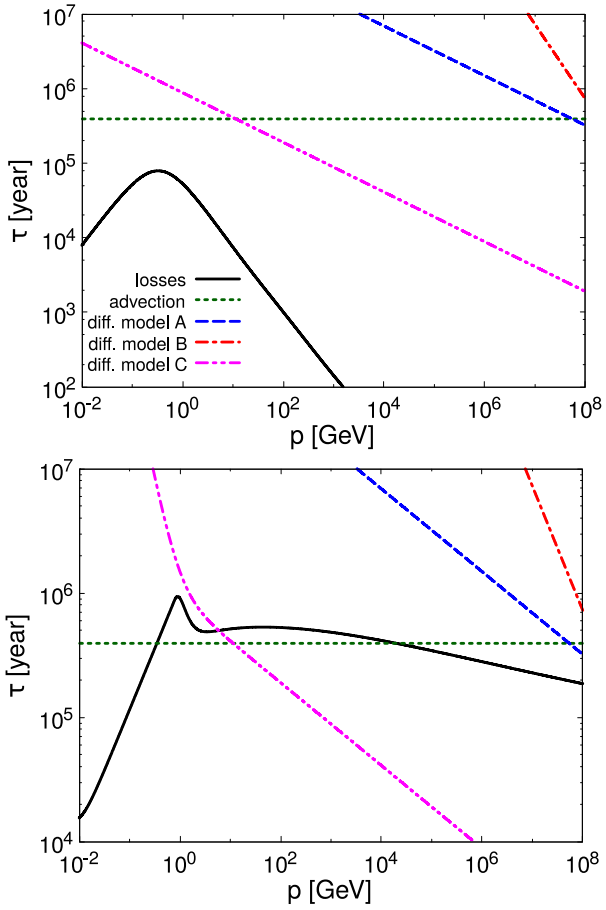

Figure 1. Energy dependence of the characteristic time-scales (expressed in years) of cosmic ray electrons (upper panel) and protons (lower panel) for the parameters of our reference case. The black thick lines represent energy losses; the green dotted lines show the advection time-scales. The time-scales of diffusion are represented by the blue dashed lines in the case of Kolmogorov, the red dot–dashed lines in the case of Bohm, and the magenta dot–dot–dashed lines in the MW-like case.

where $K_\pi \sim 0.17$ is the fraction of kinetic energy transferred from the parent proton to the single pion. $n_{\rm p}(E)$ is the proton distribution function in energy, which is linked to the distribution in momentum by $n_{\rm p}(E){\rm d}E = 4\pi p^2 f_{\rm p}(p){\rm d}p$. The secondary electron injection (here, we refer to electrons as the sum of secondary electrons and positrons) is then computed as follows:

$$q_{\rm e}(E_{\rm e}) = 2\int_{E_{\rm e}}^{\infty} q_\pi(E_\pi)\tilde{f}_{\rm e}\left(\frac{E_{\rm e}}{E_\pi}\right)\frac{{\rm d}E_\pi}{E_\pi}, \quad (10)$$

where $\tilde{f}_{\rm e}$, defined in equations (36–39) of Kelner et al. (2006), is reported in Appendix B. As we discuss next, gamma-rays are also produced as a result of the production and decay of neutral pions.

As illustrated in Table 1, the density of FIR photons is large enough that the opacity for photons above threshold for pair production is $\tau_{\gamma\gamma} \gg 1$ (see discussion in Appendix D), so that photons with $E_\gamma \gtrsim 10\,{\rm TeV}$ are absorbed inside the SBN, and give rise to $e^\pm$ pairs that we refer to as *tertiary electrons*.

The rate of injection of tertiary electrons is calculated using the leading particle approximation suggested by Aharonian, Bergström & Dermer (2013). The corresponding spectrum of injected pairs is

$$q_{\rm e}(E,r) = \int {\rm d}\epsilon\, n_{\rm bkg}(\epsilon) n_\gamma(E,r)\sigma_{\gamma\gamma}(E,\epsilon)c$$
$$= n_\gamma(E,r)c\tau_{\gamma\gamma}(E)/R, \quad (11)$$

where $n_{\rm bkg}(\epsilon)$ is the target background photon density and $n_\gamma(E)$ is the gamma-ray photon density, related to the photon emissivity through the expression $\epsilon_\gamma(E,r) \approx n_\gamma(E,r)c/(4\pi R)$, which accounts for π_0 decay, SYN, IC, and bremsstrahlung emission of electrons. All these radiation mechanisms are discussed in the following subsection.

The $p\gamma$ interaction could also provide a contribution to secondary electrons, provided the maximum energy of CR protons is higher than $\sim 1.5 \times 10^8$ GeV, a case that we do not consider here, but could retain some interest in other contexts.

The equilibrium spectrum of secondary (and tertiary) electrons is calculated by solving equation (1). However, since for electrons energy losses are always dominant, the equilibrium spectrum is well approximated by $f_{\rm sec,e}(p) = q_{\rm e}(p)\tau_{\rm loss}(p)$. Such approximation is also valid for tertiary electrons above the production threshold. Nevertheless, below such threshold the spectrum is not vanishing but is populated by electrons that lose energy during the propagation. To account also for this component, we calculate the spectrum of tertiary electrons as

$$f_{\rm ter,e}(E) = \frac{\tau_{\rm loss}(E)}{E}\int_E^\infty E' q_{\rm e}(E'){\rm d}E' \quad (12)$$

where $q_{\rm e}$ is taken from equation (11).

We also computed the production rate of neutrinos from pp interactions, following the approach proposed by Kelner et al. (2006), where the muon neutrino injection was written as

$$q_{\nu_\mu}(E) = 2\int_0^1 \left[f_{\nu_\mu^{(1)}}(x) + f_{\nu_\mu^{(2)}}(x)\right] q_\pi\left(\frac{E}{x}\right)\frac{{\rm d}x}{x}, \quad (13)$$

with $x = E/E_\pi$ and the functions $f_{\nu_\mu^{(1)}}$ and $f_{\nu_\mu^{(2)}}$, as reported in Appendix B, describe muon neutrinos produced by the direct decay $\pi \longrightarrow \mu\nu_\mu$ and by the muon decay $\mu \longrightarrow \nu_\mu\nu_e e$, respectively. The latter process also produces electron neutrinos that are described by the same equation (13) where the square bracket is replaced with the function $f_{\nu_{\rm e}}$ (see Appendix B). During propagation over cosmological distances, neutrino oscillations lead to equal distribution of the flux among the three flavours.

2.2 Non-thermal radiation from SBNi

Neutral pion decay is the leading process for the production of gamma-rays in SBNi. Following the approach of Kelner et al. (2006), we calculate the photon emissivity in the following way:

$$4\pi\,\epsilon_\gamma(E) = 2\int_{E_{\rm min}}^\infty \frac{q_\pi(E_\pi)}{\sqrt{E_\pi^2 - m_\pi^2 c^4}}{\rm d}E_\pi, \quad (14)$$

where $E_{\rm min} = E + m_\pi^2 c^4/(4E)$ and q_π are defined in equation (9).

The emissivity due to bremsstrahlung is calculated here following (Stecker 1971):

$$4\pi\,\epsilon_{\rm brem}(E) = \frac{n_{\rm ISM}\sigma_{\rm brem}c}{E}\int_E^\infty N_{\rm e}(E_{\rm e},r){\rm d}E_{\rm e}, \quad (15)$$

where $\sigma_{\rm brem} \approx 3.4 \times 10^{-26}\,{\rm cm}^2$.

The SYN emissivity is calculated using the simplified approach proposed by Ghisellini (2013), namely assuming that all energy is

radiated at the critical frequency, $\nu_{\rm syn} = \gamma^2 eB/2\pi m_e c$:

$$4\pi\,\epsilon_{\rm syn}(\nu){\rm d}\nu = P_{\rm syn}(\gamma)N_{\rm e}(\gamma){\rm d}\gamma \qquad (16)$$

$$\gamma = \sqrt{\frac{\nu}{\nu_{\rm syn}}}\ \frac{{\rm d}\gamma}{{\rm d}\nu} = \frac{\nu^{-1/2}}{2\nu_{\rm syn}^{1/2}},$$

where $P_{\rm syn}$ is the total power emitted by a single electron (Rybicki & Lightman 1986; Longair 2011; see Appendix A).

The low-energy background thermal radiation plays a very important role both as a target for ICS and for $\gamma\gamma$ absorption and pair production. We model the dust thermal contribution in the FIR domain with a diluted blackbody (DBB) as proposed by Yun & Carilli (2002) and Persic et al. (2008), or possibly a combination of them in order to model different kinds of dust emitting at different temperatures. The single-temperature DBB has the following expression:

$$n_{\rm FIR}(E) = C_{\rm dil}\frac{8\pi}{(hc)^3}\frac{E^2}{\exp^{E/kT}-1}\left(\frac{E}{E_0}\right)^{\sigma}. \qquad (17)$$

This functional shape allows the dust spectrum to be a pure blackbody above the energy E_0, whereas at lower energies it reduces to a grey body spectrum $\propto E^{2+\sigma}$, where the dust spectral index σ generally assuming values between 0 and 2 (see Yun & Carilli 2002). The normalization $C_{\rm dil}$ is obtained from a fit to the IR spectrum of SBGs, while the stellar contribution, treated as a standard blackbody, is obtained fitting the optical spectrum. We notice that, for the cases considered in Section 4, we need three different IR (dust) components and one optical component. The presence of three separate populations of dust is probably unphysical, but here are used to provide a good fit to the spectra.

The emissivity of ICS (see Jones 1968) is computed under the assumption that the low-energy background photon field is concentrated at the peak $\epsilon_{\rm peak}$ of the dust and starlight components. This approximation leads a factor $\sim$2 of uncertainty in the predicted IC flux. We consider this uncertainty as acceptable since IC is subdominant compared to other channels. Within this approximation the IC emissivity is given by

$$4\pi\,\epsilon_{\rm IC}(E,\epsilon_{\rm peak},r) = \frac{3c\sigma_{\rm T}}{4}\frac{U_{\rm rad}}{\epsilon_{\rm peak}^2}$$

$$\int_{p_{\rm min}}^{\infty} f_{\rm e}(p,r)\left[\frac{m_{\rm e}c^2}{E_{\rm e}(p)}\right]^2 G\,(q,\Gamma)\,4\pi p^2{\rm d}p, \qquad (18)$$

where $U_{\rm rad}$ is the energy density of the thermal component, $f_{\rm e}(p, r)$ is the electron distribution function (primary+secondaries), $p_{\rm min}$ is the momentum corresponding to the threshold energy $E_{\rm e}$ such that $E_{\rm e} = E/2\left[1+\left(1+m_{\rm e}^2c^4/(E\epsilon_{\rm peak})\right)^{1/2}\right]$. The function $G(q, \Gamma)$ and the variables q and Γ are reported in Appendix A. The luminosity of each thermal component 'i' is computed as $U_{{\rm rad},i} = 9L_i/(16\pi R^2 c)$, namely assuming that the spherical SBN is not opaque at those wavelengths (see also Ghisellini 2013, section 1.6).

Gamma-rays with energy above threshold for pair production may be absorbed inside the SBN, and in turn lead to the production of (tertiary) electrons (and positrons). In the same way, low-frequency radiation may be absorbed due to free–free absorption whose emissivity is given by

$$\epsilon_{\rm ff}(E) = 6.8\times10^{-38}T^{-1/2}Z^2n_{\rm e}n_i{\rm e}^{-E/kT}\bar{g}_{\rm ff}, \qquad (19)$$

where $\bar{g}_{\rm ff}$ is the mean Gaunt factor (Novikov & Thorne 1973; Rybicki & Lightman 1986) in a plasma with temperature T, Z is the electric charge of the plasma elements, namely protons and electrons (with densities $n_i = n_{\rm e}$).

In order to account for absorption, the flux of radiation escaping the SBN is calculated by solving the radiative transfer equation in the whole starburst nucleus (see e.g. Rybicki & Lightman 1986):

$$\frac{{\rm d}I(E,s)}{{\rm d}s} = \epsilon(E) - I(E,s)\eta(E), \qquad (20)$$

where η is the absorption coefficient for photons of given energy E. In the high-energy part of the spectrum, it takes into account $\gamma\gamma$ absorption, $\eta = \eta_{\gamma\gamma} = \int\sigma_{\gamma\gamma}(E, E')n_{\rm bkg}(E'){\rm d}E'$, whereas at low energies it describes free–free absorption $\eta = \eta_{\rm ff} \approx 0.018T^{-3/2}Z^2n_{\rm e}n_i\bar{g}_{\rm ff}(h/E)^2$. The spatial coordinate s runs through the SBN at a given distance from the centre.

The intensity $I(E)$ for each line of sight across the SBN is calculated by solving numerically equation (20) then, summing up over all line of sight we get the total luminosity of the SBN.

Although redshift effects from nearby SBNi are negligible, absorption of gamma-rays at very high energies due to pair production off the diffuse background light remains important at it is accounted for following the approach of Franceschini & Rodighiero (2017; see Appendix C for the detailed description).

3 CR DIFFUSION AND CALORIMETRY

The modelling of the non-thermal activity of SBGs relies upon the assessment of the assumption of calorimetry, which is often adopted with no much discussion in most literature on the topic. In this section, we address the issue of whether CRs lose most of their energy inside SBNi or not in terms of CR transport, and we discuss the observational evidence in terms of emission of non-thermal radiation. In order to reach this goal, we compute the spectra of protons, (primary, secondary, and tertiary) electrons and the radiation emitted by them in the three diffusion models discussed earlier.

Model A is our benchmark transport model: it predicts that protons lose an appreciable fraction of their energy inside the SBN, although the time-scale for escape is comparable with that of the wind advection. The smallness of the diffusion coefficient for this model causes the advection to be the main channel of escape of CR protons from the nucleus, for energies as high as $\sim$10 PeV. The time-scale of energy losses of protons, dominated by pion production, becomes shorter than the advection time above $\sim$10 TeV because of the weak energy dependence of the cross-section for this process.

All electrons (primary, secondary from pp collisions, and tertiary) lose their energy inside the SBN, hence the assumption of calorimetry is certainly justified for the electrons.

The equilibrium spectra of protons and electrons for Model A are shown in Fig. 2 (top panel), where we adopted the reference values of parameters as listed in Table 1. The strong role of energy losses makes the spectrum of protons reflect the injection spectrum, with a small correction due to the energy dependence of losses. For electrons, energy losses are always faster than both advection and diffusion, hence their spectrum is steeper than the injection spectrum by approximately one power of energy since the main channel of losses are represented by SYN emission in the intense magnetic field of the SBN and by IC off the IR photons. Small wiggles are present in the high-energy spectrum of secondary electrons (not clearly visible in the figure due to the large vertical scale) reflecting the fact that the cross-section for ICS off photon backgrounds enters the Klein–Nishina regime when $E_\gamma\epsilon_{\rm ph} \sim m_{\rm e}^2c^4$. At energies $\lesssim$GeV, the spectrum of primary electrons is dominated by ionization losses, while for secondary electrons the low-energy part of the spectrum falls fast because of the threshold for pion production

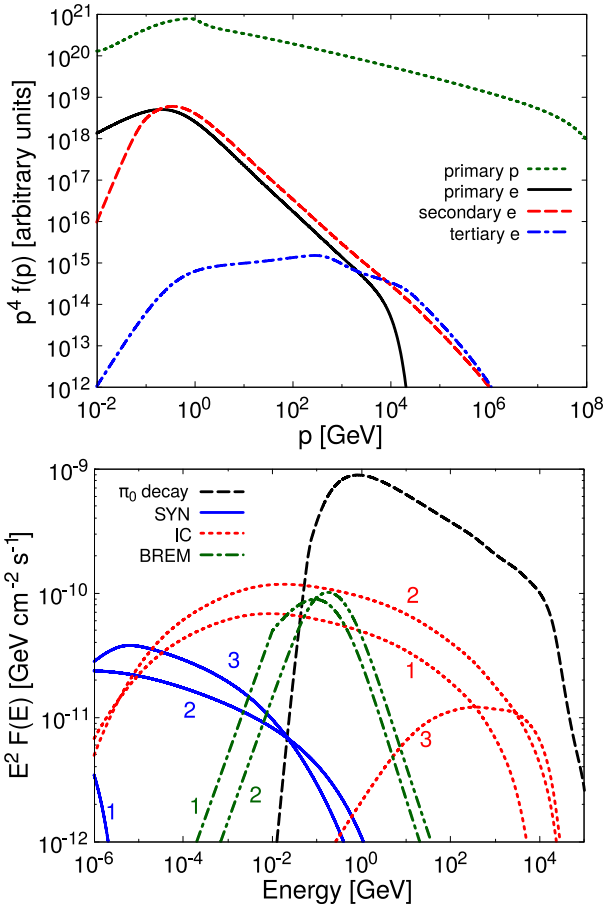

Figure 2. Particle and photon spectra in Model A. The upper panel shows primary protons (the green dashed line), primary electrons (the black thick line), secondary electrons (the red dashed line), and tertiary electrons (the blue dot–dashed line). The lower panel shows the high-energy spectral components of π_0 decay (the black dashed line), inverse Compton (the red dotted line), synchrotron (the blue thick line), and bremsstrahlung (the green dot–dashed line). The relative contributions of the different electron populations are separated in primaries (1), secondaries (2), and tertiaries (3).

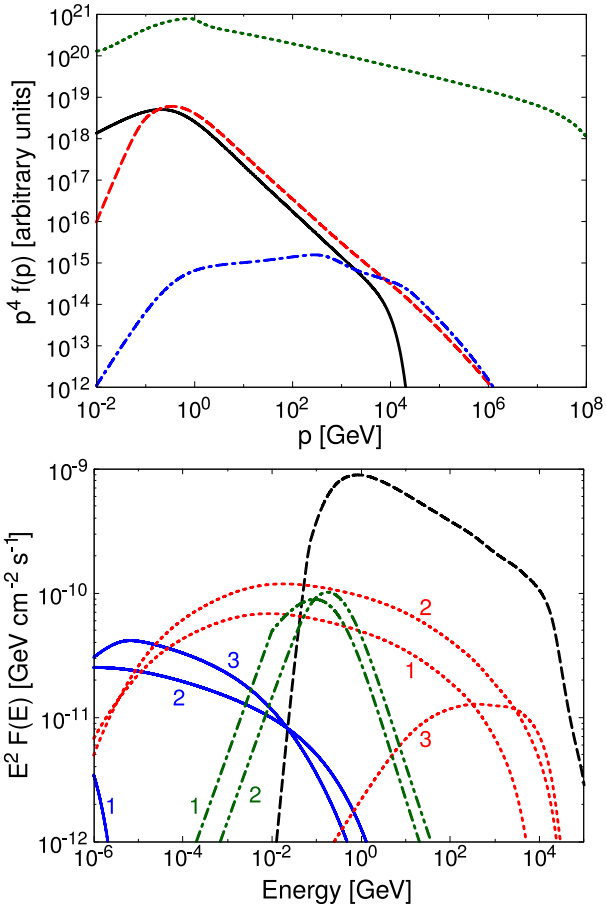

Figure 3. Particle and photon spectra in Model B. The line style is the same as in Fig. 2.

in pp collisions. Tertiary electrons, produced by pair production of high-energy gamma-rays in the SBN, start at energies ∼TeV, where absorption off the near infrared (NIR) background becomes important. A second peak is present at energies ∼20 TeV due to the peak in the FIR. On the contrary, the contribution due to optical photons is almost negligible. The spectrum of tertiary electrons at energies lower than their minimum injection energy is due to SYN and ICS ageing of tertiary electrons injected at higher energies.

The bottom panel of Fig. 2 shows the photon spectra from an SBN with the values of the parameters listed in Table 1. The number labels refer to the contribution of primary (1), secondary (2), and tertiary (3) electrons. Most gamma-rays with energy $\gtrsim$100 meV are due to production and decay of neutral pions. The cut-off in the spectrum of gamma-rays at energies ∼10 TeV is due to absorption of gamma-rays inside the SBN. For larger distances of the galaxies from the Earth, the absorption on the extragalactic background light is also expected to become important. We will discuss this point further when dealing with individual sources.

It is interesting to notice that while the SYN emission of primary electrons quickly becomes unimportant at high photon energy, the SYN emission of secondary and tertiary electrons is dominant in the hard X-ray band. Hence, the detection of such hard X-ray emission may be considered as a rather unique signature of strong CR interactions inside the SBN and corresponding copious production of secondary electrons and even efficient gamma-ray absorption (tertiary electrons).

In the soft gamma-ray band, most emission is due to a combination of ICS and bremsstrahlung of primary and secondary electrons and to SYN emission of secondary and tertiary electrons.

In Fig. 3, we show the particle (upper panel) and the photon spectrum (lower panel) in the context of Model B, where Bohm diffusion was assumed. Although the time-scale for diffusion in Model B is typically much shorter than for Model A, not much difference is observed in the predicted spectra, as a result of the fact that in both models the transport of CRs is mostly dominated by advection and energy losses. Electrons are well confined inside the SBN and lose all their energy inside the nucleus. These two conditions imply that calorimetry is a good approximation for both Models A and B, hence much of what has been said for Model A also applies to Model B.

Model C is qualitatively different from previous diffusion models, in that the larger diffusion coefficient determines a transition from advection- to diffusion-dominated transport at $E \sim 1$ GeV for protons, while electrons remain loss dominated. The corresponding results are shown in Fig. 4. The spectrum of CR protons is steeper than injection by an amount determined by the energy dependence of the diffusion coefficient (1/3) and, as a consequence, the injection spectrum of secondary electrons is correspondingly steeper as

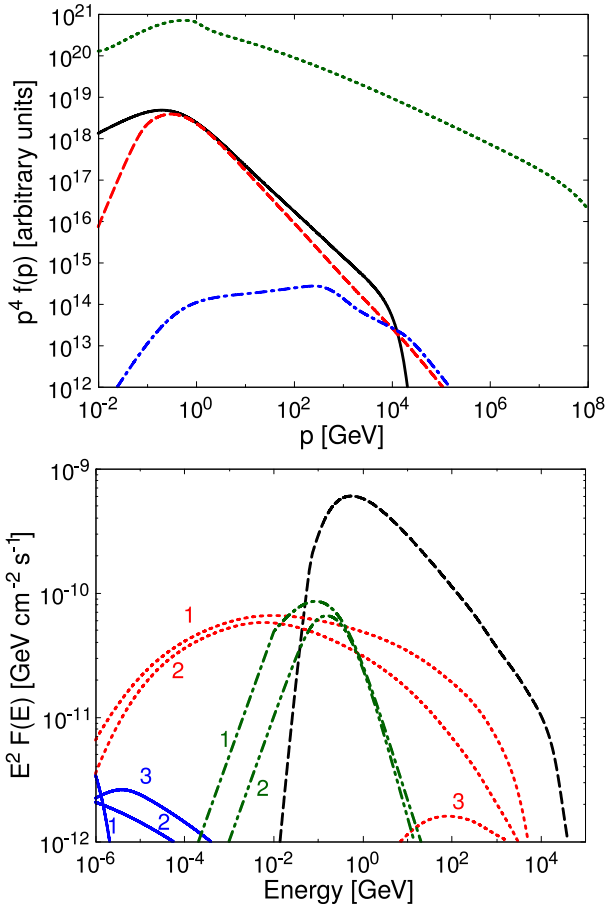

Figure 4. Particle and photon spectra in Model C. The line style is the same as in Fig. 2.

$E^{-(2.25+1/3)}$. Moreover, the shorter diffusion time leads to a smaller density of secondary electron when compared with the results of Models A and B, so that the electron spectrum is now dominated by primary electrons. The main imprints on the spectrum of photons (lower panel) are the steeper spectrum of gamma-rays from π^0 decays and the fact that the SYN emission in the hard X-ray band is sizeably smaller than for Models A and B, as a result of the lack of calorimetry for CR protons.

The different emission in the hard X-ray band between Models A and B on one hand and Model C on the other illustrate well the potential importance of the detection of hard X-rays from SBNi, in that such photons carry information about the calorimetric properties of the SBN. Although hard X-rays from the cores of SBGs have been observed (Strickland & Heckman 2007; Wik et al. 2014; Paggi et al. 2017), an important contribution to such diffuse emission is typically attributed to unresolved X-ray binaries, SNRs, *O* or early-*B* spectral type stars, diffuse thermal plasma, and a possible AGN activity (for a detailed discussion of these components see Persic & Rephaeli 2002). CR electrons are also expected to contribute to the diffuse hard X-ray emission mainly through ICS on the IR background (see Persic & Rephaeli 2002). The possibility that a contribution to the diffuse hard X-ray flux could come from SYN emission of CR electrons was first suggested by Lacki & Thompson (2013). Nevertheless, in their model the X-ray emission is dominated by IC from primary electrons and is roughly 10 times smaller than our prediction in the same energy band, which is, instead, dominated by SYN emission from secondary and tertiary electrons. In their case, the contribution from secondary electrons is much smaller due to a faster diffusion of protons. Indeed, as we discussed earlier, the contribution of secondary and tertiary electrons to the diffuse hard X-ray emission reflects the effectiveness of the confinement of CRs inside SBNi, which in turn can be expressed in terms of luminosity in some selected bands.

Table 2. Luminosity (expressed in units of 10^{38} erg s^{-1}) in three selected energy bands in Models A, B, and C. L_γ is the gamma-ray luminosity computed in the energy range 0.1–10^2 GeV, whereas $L_{\rm IR}$ is computed in the far-infrared (8 μm $< \lambda <$ 10^3 μm). $L_{\rm X}$ is computed in the X-ray channel 1–10^2 keV, whereas $L_{\rm X_1}$, $L_{\rm X_2}$, and $L_{\rm X_3}$ are computed in the sub-bands 1–8, 4–25, and 25–100 keV, respectively. The square brackets show separately the contribution of SYN and IC to the total luminosity (value out of the parentheses).

	Model A	Model B	Model C
L_γ	162	163	94
$L_{\rm IR}$	1.65×10^6	1.65×10^6	1.65×10^6
$L_{\rm X}$	13.6 [7.1, 6.5]	14.3 [7.8, 6.5]	5.6 [0.5, 5.1]
$L_{\rm X_1}$	4.8 [3.4, 1.4]	5.1 [3.7, 1.4]	1.5 [0.3, 1.2]
$L_{\rm X_2}$	5.4 [3.0, 2.4]	5.7 [3.2, 2.5]	2.1 [0.2, 1.9]
$L_{\rm X_3}$	5.3 [2.0, 3.3]	5.5 [2.2, 3.3]	2.6 [0.1, 2.5]

In Table 2, we show the luminosity in gamma-rays (0.1–10^2 GeV), X-rays (1–10^2 keV), and IR radiation (8–10^3 μm). Models A and B basically return the same result. On the other hand, Model C shows a clear reduction in the X-ray and gamma-ray luminosity by about a factor $\sim 2 \div 3$, while the IR luminosity remains unchanged since the thermal contribution dominates upon SYN by $\sim$5 orders of magnitudes. For completeness, in the same table, we also report the X-ray luminosities in three bands, 1–8 keV (typical of Chandra), at 4–25 keV (typical of NuStar), and 25–10^2 keV. Clearly, the SYN emission of secondary and tertiary electrons can contribute (together with the XRBs component) to provide a natural explanation of the hard X-ray extra-component in the band 0.5–10 keV discussed in Persic & Rephaeli (2002).

4 APPLICATION TO KNOWN SBGS

In this section, we specialize our calculation to the case of the three nearby SBGs, namely NGC 253, M82 (respectively, with $D_{\rm L} \approx 3.8$ and $D_{\rm L} \approx 3.9$ as found by Rekola et al. 2005 and Sakai & Madore 1999), and Arp220 (located at $D_{\rm L} \approx 77$ Mpc, as inferred by Scoville et al. 1998). The latter belongs to the ULIRG class, characterized by very prominent IR luminosity, higher ISM density, and magnetic field energy density and more intense star formation activity (Scoville et al. 2015). Arp220 shows a rate of SN explosions that is more than one order of magnitude higher than typical SBGs (Mannucci et al. 2003; Lonsdale et al. 2006).

For the modelling of the emission from these SBGs, we start by fitting the thermal emission, in the $\sim$0.1 meV–few eV range, assuming that the observed emission in this band is dominated by the SBN and then we tune the other parameters to fit the multiwavelength spectra, from radio to gamma-rays. The parameters' values used for each source are listed in Table 3.

We check a posteriori that the best-fitting values of the parameters are in agreement with values reported in the literature. In particular, the inferred radius of the SBN and the ISM conditions appears to compare well with the values presented by Sakamoto et al. (2011) and Hailey-Dunsheath et al. (2008) for NGC 253; Förster Schreiber et al. (2003) and Förster Schreiber et al. (2001) for M82. For Arp220, we adopt a simplified spherical geometry embedding the two

Table 3. Input parameters for the galaxies examined in Section 4.

Parameters	NGC 253	M82	Arp220
D_L (Mpc) [z]	3.8 [8.8 10^{-4}]	3.9 [9 10^{-4}]	77.0 [1.76 10^{-2}]
$\mathcal{R}_{SN}$ (yr^{-1})	0.027	0.05	2.25
R (pc)	150	220	250
α	4.3	4.25	4.45
B (μG)	170	210	500
M_{mol} (10^8 $M_\odot$)	0.88	1.94	57
n_{ISM} (cm^{-3})	250	175	3500
n_{ion} (cm^{-3})	30	22.75	87.5
v_{wind} ($km\,s^{-1}$)	300	600	500
T_{plasma} (K)	8000	7000	3000
$U^{FIR}_{eV\,cm^{-3}}$ [$\frac{kT}{meV}$]	1958 [3.5]	910 [3.0]	31321 [3.5]
$U^{MIR}_{eV\,cm^{-3}}$ [$\frac{kT}{meV}$]	587 [8.75]	637 [7.5]	9396 [7.0]
$U^{NIR}_{eV\,cm^{-3}}$ [$\frac{kT}{meV}$]	587 [29.75]	455 [24.0]	125 [29.75]
$U^{OPT}_{eV\,cm^{-3}}$ [$\frac{kT}{meV}$]	2936 [332.5]	546 [330.0]	1566 [350.0]

Table 4. Inferred values for the luminosity at different energies and energy density of magnetic field and non-thermal particles for the examined galaxies.

Outcomes	NGC 253	M82	Arp220
$E_{SN}\xi_{CR}$ ($erg\,s^{-1}$)	8.56×10^{40}	1.59×10^{41}	7.14×10^{42}
$L_{0.1-10^2\,GeV}$ ($erg\,s^{-1}$)	1.31×10^{40}	1.82×10^{40}	1.36×10^{42}
$L_{1-10^2\,keV}$ ($erg\,s^{-1}$)	0.81×10^{39}	1.51×10^{39}	9.91×10^{40}
$L_{8-10^3\,\mu m}$ ($erg\,s^{-1}$)	1.65×10^{44}	2.27×10^{44}	6.51×10^{45}
U_B ($eV\,cm^{-3}$)	717.71	1095.19	6208.54
U_p ($eV\,cm^{-3}$)	655.63	413.29	1323.91
U_e ($eV\,cm^{-3}$)	5.06	3.41	14.35
$U_{e,sec}$ ($eV\,cm^{-3}$)	6.15	3.92	15.78
$U_{e,ter}$ ($eV\,cm^{-3}$)	3.48×10^{-3}	1.49×10^{-3}	2.65×10^{-3}

galactic nuclei that are observed. In fact, we have adopted parameters that are a reasonable average between the highly compact SBNi and their surrounding environment (detailed observations of Arp220 and its ISM condition are discussed in Scoville et al. 2015 and Sakamoto et al. 1999). Parameters such as the average magnetic field and the advection speed have been taken consistently with typical values expected from SBNi (see e.g. Thompson et al. 2006a and Heckman & Thompson 2017, respectively).

For all three sources analysed in this section, radio data in the frequency range 1–10 GHz are taken from Williams & Bower (2010), whereas data at higher energies, namely from ∼0.1 meV to ∼10 eV, have been retrieved from the NED[1] catalog (in particular, we use the SED-builder online tool https://tools.ssdc.asi.it/). In all cases, we use three DBBs for the dust contribution, a normal BB for the stellar component, and a free–free contribution from the thermal plasma. The parameters of these low-energy components are listed in the last five rows of Table 3, while Table 4 summarizes the main outcomes of our modelling for all the three SBNi. Next, we briefly describe our findings related to the three chosen SBG and we draw some general conclusions.

NGC 253: The nuclear region of NGC 253 is very compact and luminous at optical wavelength. This causes a non-negligible $\gamma\gamma$ absorption at energies of few hundred GeV, which in turn determines

[1]The NASA/IPAC Extragalactic Database (NED) is operated by the Jet Propulsion Laboratory, California Institute of Technology, under contract with the National Aeronautics and Space Administration.

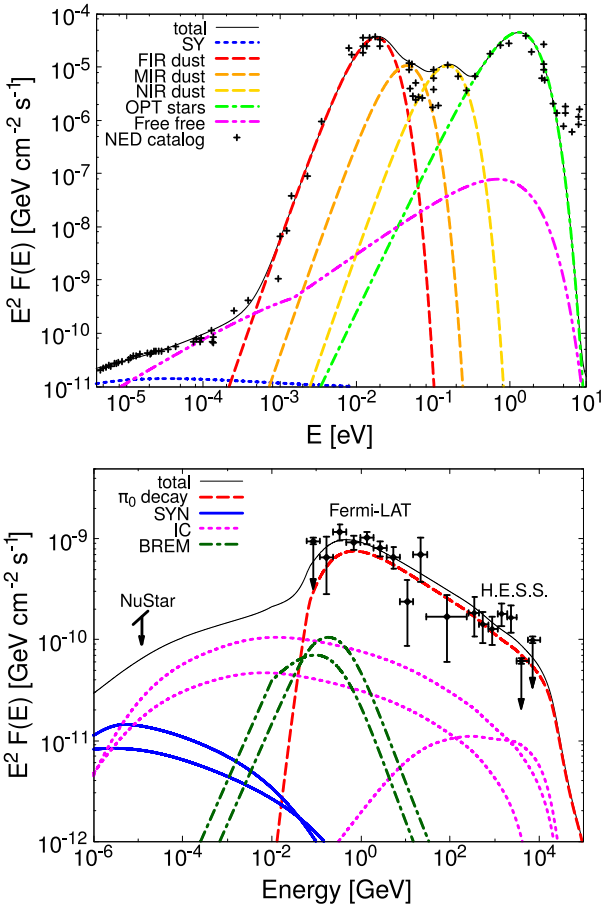

Figure 5. Multiwavelength spectrum of NGC 253. Upper panel shows the low-energy spectrum with relative components: thermal dust DBBs (the dashed red, orange, and yellow line), optical star BB (the green dot–dashed line), thermal free–free (the magenta dot–dot–dashed line), and SYN (the blue dotted line). Lower panel shows the high-energy spectral components: π_0 (the red dashed line), IC (the magenta dotted lines), BREM (the green dot–dashed lines), and SYN (the blue thick lines). Together with the photons, we show the single flavour neutrino flux (the thin gold dashed line). The data (the black points) are observed by *Fermi*–LAT and HESS and presented in Abdalla et al. (2018) for the HE and VHE domain, whereas the hard X-ray upper limit is taken from Wik et al. (2014).

a softening of the gamma-ray spectrum already below ∼1 TeV. The spectrum above 100 meV is totally dominated by the π_0 component. Below ∼100 meV, the dominant emission mechanism is IC (mainly from secondary electrons). Only at keV energies, the IC emission becomes comparable with the SYN components from secondary and tertiary electrons. Relativistic bremsstrahlung is always subdominant but provides a non-negligible contribution to the total gamma-ray emission in the range $10 \div 100$ meV.

The multifrequency spectrum of NGC 253 is shown in Fig. 5. The top panel illustrates the good agreement between the results of our modelling of the low-energy emission and observations. The bottom panel is more interesting in that it shows the gamma-ray emission coming from both the decays of neutral pions and from interactions of electrons and gamma-rays with magnetic fields and low-energy photon background inside the SBN.

Gamma-ray data collected by Fermi-LAT and HESS (see Abdalla et al. 2018) are well reproduced. Of particular interest is the shape of the spectrum below ∼1 GeV where data show a strong hint of the

pion bump, a clear signature of the hadronic origin of gamma-rays. The computed hard X-ray flux, contributed by both SYN and IC, is at the level of $E^2F(E) \approx 10^{-10}$ GeV cm^2 s^{-1} at 10 keV, appreciably larger than previous estimates (e.g. Lacki & Thompson 2013), but consistent with detailed observations of the nuclear region of NGC 253 performed by NuStar (Wik et al. 2014). In this case, our larger flux with respect to Lacki & Thompson (2013) is mainly due to the IC emission from secondary electrons copiously produced because the larger confinement time of CRs, whereas SY dominates only below ∼5 keV.

M82: The multiwavelength spectrum of M82 is very similar to that of NGC 253, but requires a slight harder injection (see Table 3) to explain the harder observed gamma-ray spectrum. In this way, the gamma-ray observations from *Fermi*–LAT and Veritas (see e.g. Acciari et al. 2009; Ackermann et al. 2012) are again well reproduced. The absorption of VHE gamma-rays is almost negligible below a few TeV because the optical background is almost a factor 5 lower at the peak with respect to the case of NGC 253.

The computed diffuse hard X-ray flux is again very high ($E^2F(E) \approx 10^{-10}$ GeV cm^{-2} s^{-1} at a few keV) and, different from NGC 253, it is dominated by SYN emission of secondary and tertiary electrons up to ∼20 keV. Although no measurement of the truly diffuse hard X-ray flux from the nuclear region of M82 is available at present, recent observations carried out using *Chandra* (see Strickland & Heckman 2007), *XMM–Newton* (see Ranalli et al. 2008) and more recently NuStar (Bachetti et al. 2014) suggest that our computed hard X-ray diffuse flux is ≈5 per cent ÷ 10 per cent of the total observed flux in the energy band 3–8 keV, hence we interpret the X-ray point in Fig. 6 as an upper limit to the diffuse emission since point-like sources could contaminate such measurement.

Arp220: Our simple assumptions on the geometric properties of the SBN are particularly restrictive when applied to a source such as Arp220, with its complex morphology (two nuclei and possibly a low-activity AGN). In this sense, it is noteworthy that, despite such limitations, a reasonable fit to the multifrequency emission can be obtained for this sources, using the input parameters listed in the last column of Table 3. In particular, we have found that our best-fitting value for the magnetic field (∼500 μG) is about a factor 2 lower than the typical ∼mG field assumed in literature for the two SBNi of Arp220 (see e.g. Thompson et al. 2006b; Barcos-Mu noz et al. 2015; McBride et al. 2015; Yoast-Hull et al. 2017). Our value for the magnetic field is not in tension with previous estimates because it represents an average between the magnetic field inside the two nuclei and the one in the surrounding region, estimated to be $\sim 10^2$ μG (for similar discussions, see also Torres 2004; Varenius et al. 2016).

The multifrequency spectrum of Arp220 is shown in Fig. 7. Gamma-ray observations (see Peng et al. 2016) suggest that Arp220 requires a softer injection slope with respect to normal starbursts such as NGC 253 and M82. In alternative, one could speculate that the level of turbulence in Arp220 is lower so as to make CR transport dominated by diffusion. However, this possibility does not seem to sit well with the observed level of activity of this source. On the other hand, it is not easy to envision the reason why one should expect a steeper injection spectrum. In the absence of better indications, here we just assume a steeper injection spectrum.

The dominant gamma-ray component above ∼100 meV is again the π_0 decay, whereas at lower energies only ICS and bremsstrahlung emissions are expected to be relevant. Moreover, different from normal starbursts, the SYN component is completely

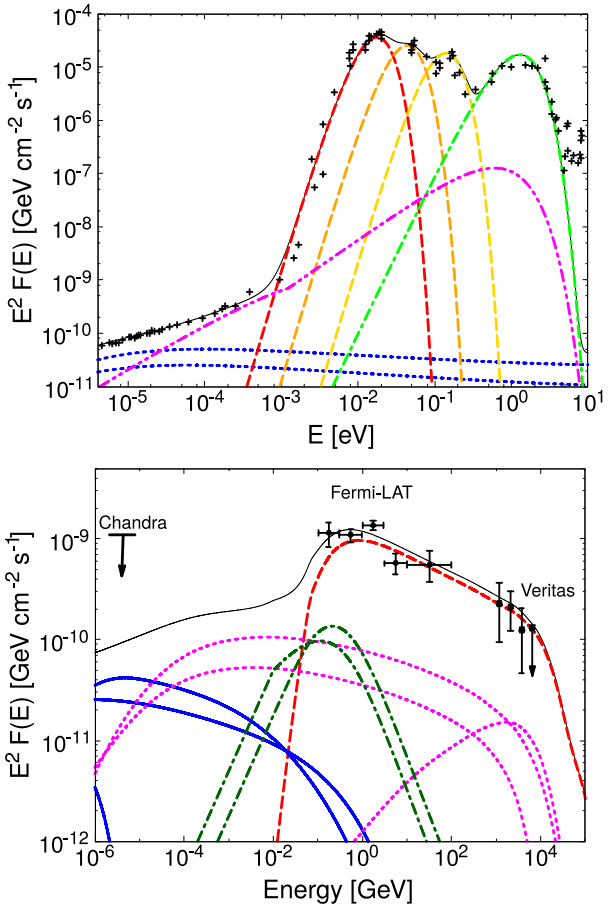

Figure 6. Multiwavelength spectrum of M82. The line style is the same of Fig. 5. The HE gamma-ray observation are taken from the *Fermi*–LAT observation discussed in Acero et al. (2015), whereas VHE data come from Veritas and are published in Acciari et al. (2009). The X-ray point is a *Chandra* (see Strickland & Heckman 2007) we have taken as upper limit because of possible contamination from undetected point-like sources (e.g. XRBs) and thermal plasma.

negligible in the whole high-energy part of the photon spectrum (see lower panel of Fig. 7).

The diffuse hard X-ray flux from the central region of Arp220 has been investigated by Paggi et al. (2017). Taking into account that we are modelling the core of Arp220 as a unique region we show their measured X-ray luminosity coming from the central 4.5 arcsec, corresponding to a radius of ∼840 pc that also accounts for the region between the two nuclei (see X-ray upper limit in the lower panel of Fig. 7). As for the other two SBNi analysed above, we take this measured luminosity as an upper limit for our non-thermal X-ray flux because of possible contamination from point-like sources. Indeed, after converting the measured luminosity in a differential flux assuming an energy slope of −1.6, we find out that the measured flux is located above our computed spectrum, as expected.

The application of our calculations of CR transport to individual SBGs allows us to draw some general conclusions: (1) in all cases we considered, observations show that CR protons lose an appreciable fraction of their energy inside the SBN; (2) from the point of view electrons, the SBN is an excellent calorimeter. (3) Most of the emission at frequencies other than high-energy gamma-rays is dominated by secondary electrons, products of pp collisions.

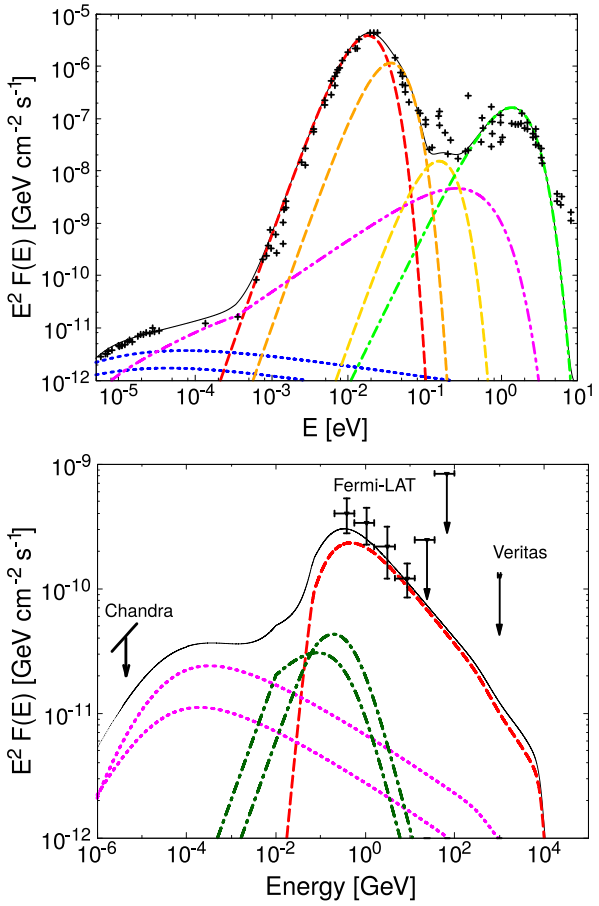

Figure 7. Multiwavelength spectrum of Arp220. The line stile is the same of Fig. 5. Gamma-ray data are taken from Peng et al. (2016), whereas the X-ray point (which again we take as upper limit for our diffuse flux taking into account possible contamination from point-like sources and thermal plasma) has been taken from Paggi et al. (2017).

(4) Electron–positron pairs are effectively generated because of the absorption of high-energy gamma-rays with the background light in the SBN. The absorption of gamma-rays inside the nucleus inhibits the development of an electromagnetic cascade during propagation, which might have important implications for the sources of high-energy neutrinos; (5) The SYN emission of secondary and tertiary electrons generates a diffuse hard X-ray emission that can be envisioned as a unique diagnostic to investigate the calorimetric properties of SBGs.

More detailed observations of gamma-ray emission from SBGs with upcoming telescopes, and in particular with the Cherenkov Telescope Array (see Cherenkov Telescope Array Consortium 2017), will certainly shed new light on the physical processes at work in SBGs.

The single-flavour neutrino fluxes are well described by power laws in energy of index $\alpha - 2$. The flux normalization at 10^2 TeV obtained for NGC 253 and M82 is roughly 10^{-11} GeV cm^{-2} s^{-1}, and it is about a factor 50 lower for Arp220. Considering that the point-like source sensitivity for IceCube and KM3NeT allows for the detection of a neutrino flux two orders of magnitude higher than what we obtained for NGC 253 and M82 (see Aartsen et al. 2017; Aiello et al. 2018), the probability of detecting a nearby SBN as an isolated neutrino source is very small.

5 CONCLUSIONS

We have modelled SBNi as leaky box systems assuming spherical symmetry and homogeneous properties of the medium. We have investigated how different diffusion coefficients change the high-energy spectra modifying the normalization and the slope in the energy range above GeV and determining an enhanced flux in the hard X-ray energy band. We have found that in the most likely diffusion scenario, which is described by a Kolmogorov diffusion coefficient assuming $\delta B/B \approx 1$ and typical length of perturbation $L_0 \approx 1$ pc, the escape is completely provided by the wind advection up to PeV energies. At higher energies, the time-scale at which particles can diffuse away could become comparable with advection and energy losses.

Normal starbursts such as NGC 253 and M82 are consistent with a slope of injection $\alpha \approx 4.2 \div 4.3$ and the softening taking place in the high-energy part of their photon spectra can be explained by the $\gamma\gamma$ absorption. On the other hand, the ULIRG class Arp220 is compatible with a softer injection $\alpha = 4.45$. Moreover, in agreement with the results obtained in Yoast-Hull, Gallagher & Zweibel (2016), the galaxies we have analysed are consistent with a sub-equipartition between the energy density of CR-particle and the magnetic field, namely $U_p/U_B \approx 0.9$, 0.4, and 0.2 for NGC 253, M82, and Arp220, respectively. The ratio between the gamma-ray luminosity and the total injected energy in CRs ($\geq$1/10) suggests that proton calorimetry is at least partially achieved in NGC 253 and M82, whereas Arp220 seems to be able to better confine particles (showing a ratio $\sim$1/5).

The neutrino flux from individual SBNi was found to be well below the point source sensitivity of current neutrino telescopes. On the other hand, as pointed out by Loeb & Waxman (2006), Lacki et al. (2011), Tamborra et al. 2014, and Bechtol et al. 2017, the contribution of SBNi to the diffuse neutrino flux might be relevant. The implications of the CR confinement studied in this paper for the diffuse neutrino flux will be discussed in an upcoming article.

ACKNOWLEDGEMENTS

This research has used the NASA/IPAC Extragalactic Database (NED), which is operated by the Jet Propulsion Laboratory, California Institute of Technology, under contract with the National Aeronautics and Space Administration.

REFERENCES

Aartsen M. G. et al., 2017, preprint (arXiv:1710.01179)
Abdalla H. et al., 2018, A&A, 617, A73
Acciari V. A. et al., 2009, Nature, 462, 770
Acero F. et al., 2015, ApJS, 218, 23
Ackermann M. et al., 2012, ApJ, 755, 164
Aharonian F., Bergström L., Dermer C., 2013, Astrophysics at Very High Energies: Saas-Fee Advanced Course 40. Swiss Society for Astrophysics and Astronomy, Saas-Fee Advanced Course, Vol. 40. Springer-Verlag, Berlin Heidelberg, p. 40
Aiello S. et al., 2018, preprint (arXiv:1810.08499)
Anchordoqui L. A., 2018, Phys. Rev. D, 97, 063010
Anchordoqui L. A., Romero G. E., Combi J. A., 1999, Phys. Rev. D, 60, 103001
Bachetti M. et al., 2014, Nature, 514, 202
Barcos-Mu noz L. et al., 2015, ApJ, 799, 10
Bechtol K., Ahlers M., Di Mauro M., Ajello M., Vandenbroucke J., 2017, ApJ, 836, 47
Blasi P., 2010, MNRAS, 402, 2807

Cherenkov Telescope Array Consortium, 2017, Science with the Cherenkov Telescope Array. World Scientific Press, Singapore
de Cea del Pozo E., Torres D. F., Rodriguez Marrero A. Y., 2009, ApJ, 698, 1054
Engelbracht C. W. et al., 2006, ApJ, 642, L127
Förster Schreiber N. M., Genzel R., Lutz D., Kunze D., Sternberg A., 2001, ApJ, 552, 544
Förster Schreiber N. M., Genzel R., Lutz D., Sternberg A., 2003, ApJ, 599, 193
Franceschini A., Rodighiero G., 2017, A&A, 603, A34
Gao Y., Solomon P. M., 2004, ApJ, 606, 271
Ghisellini G., ed., 2013, Lecture Notes in Physics, Vol. 873, Radiative Processes in High-energy Astrophysics. Springer Verlag, Berlin
Hailey-Dunsheath S., Nikola T., Stacey G. J., Oberst T. E., Parshley S. C., Bradford C. M., Ade P. A. R., Tucker C. E., 2008, ApJ, 689, L109
Heckman T. M., Thompson T. A., 2017, in Athem W. Alsabti, Paul Murdin, eds, A Brief Review of Galactic Winds, Handbook of Supernovae. Springer, Berlin
Jones F. C., 1968, Phys. Rev., 167, 1159
Kelner S. R., Aharonian F. A., Bugayov V. V., 2006, Phys. Rev. D, 74, 034018
Lacki B. C., Thompson T. A., 2013, ApJ, 762, 29
Lacki B. C., Thompson T. A., Quataert E., Loeb A., Waxman E., 2011, ApJ, 734, 107
Loeb A., Waxman E., 2006, J. Cosmol. Astropart. Phys., 0605, 003
Longair M. S., 2011, High-energy Astrophysics. Cambridge Univ. Press, Cambridge
Lonsdale C. J., Diamond P. J., Thrall H., Smith H. E., Lonsdale C. J., 2006, ApJ, 647, 185
Mannucci F. et al., 2003, A&A, 401, 519
McBride J., Robishaw T., Heiles C., Bower G. C., Sarma A. P., 2015, MNRAS, 447, 1103
Novikov I. D., Thorne K. S., 1973, in Dewitt C., Dewitt B. S., eds, Black Holes (Les Astres Occlus). Gordon and Breach, New York. p. 343
Paggi A. et al., 2017, ApJ, 841, 44
Paglione T. A. D., Marscher A. P., Jackson J. M., Bertsch D. L., 1996, ApJ, 460, 295
Peng F.-K., Wang X.-Y., Liu R.-Y., Tang Q.-W., Wang J.-F., 2016, ApJ, 821, L20
Persic M., Rephaeli Y., 2002, A&A, 382, 843
Persic M., Rephaeli Y., Arieli Y., 2008, A&A, 486, 143
Ranalli P., Comastri A., Origlia L., Maiolino R., 2008, MNRAS, 386, 1464
Rekola R., Richer M. G., McCall M. L., Valtonen M. J., Kotilainen J. K., Flynn C., 2005, MNRAS, 361, 330
Rephaeli Y., Arieli Y., Persic M., 2010, MNRAS, 401, 473
Romero G. E., Torres D. F., 2003, ApJ, 586, L33
Romero G. E., Müller A. L., Roth M., 2018, A&A, 616, A57
Rybicki G. B., Lightman A. P., 1986, Radiative Processes in Astrophysics. Wiley-VCH, New York
Sakai S., Madore B. F., 1999, ApJ, 526, 599
Sakamoto K., Scoville N. Z., Yun M. S., Crosas M., Genzel R., Tacconi L. J., 1999, ApJ, 514, 68
Sakamoto K., Mao R.-Q., Matsushita S., Peck A. B., Sawada T., Wiedner M. C., 2011, ApJ, 735, 19
Schlickeiser R., 2002, Cosmic Ray Astrophysics. Springer, Berlin
Scoville N. et al., 2015, ApJ, 800, 70
Scoville N. Z. et al., 1998, ApJ, 492, L107
Seaquist E. R., Odegard N., 1991, ApJ, 369, 320
Shopbell P. L., Bland-Hawthorn J., 1998, ApJ, 493, 129
Stecker F. W., 1971, Cosmic Gamma Rays, NASA Special Publication, Washington, p. 249
Strickland D. K., Heckman T. M., 2007, ApJ, 658, 258
Strickland D. K., Heckman T. M., 2009, ApJ, 697, 2030
Sudoh T., Totani T., Kawanaka N., 2018, PASJ, 70, 49
Tamborra I., Ando S., Murase K., 2014, J. Cosmol. Astropart. Phys., 1409, 043
Thompson T. A. et al., 2006a, ApJ, 645, 186
Thompson T. A., Quataert E., Waxman E., Murray N., Martin C. L., 2006b, ApJ, 645, 186
Torres D. F., 2004, ApJ, 617, 966
Varenius E. et al., 2016, A&A, 593, A86
Wang X., Fields B. D., 2018, MNRAS, 474, 4073
Weaver K. A., Heckman T. M., Strickland D. K., Dahlem M., 2002, ApJ, 576, L19
Wik D. R. et al., 2014, ApJ, 797, 79
Williams P. K. G., Bower G. C., 2010, ApJ, 710, 1462
Yoast-Hull T. M., 2015, PhD thesis, Univ. Wisconsin
Yoast-Hull T. M., Everett J. E., Gallagher J. S., Zweibel E. G., 2013, ApJ, 768, 53
Yoast-Hull T. M., Gallagher J. S., Zweibel E. G., 2016, MNRAS, 457, L29
Yoast-Hull T. M., Gallagher J. S., Aalto S., Varenius E., 2017, MNRAS, 469, L89
Yun M. S., Carilli C. L., 2002, ApJ, 568, 88
Zirakashvili V. N., Aharonian F., 2007, A&A, 465, 695

APPENDIX A: ENERGY LOSS TIME-SCALES

In this appendix, we summarize the formula used for the energy losses of all processes considered for both electrons and protons. The energy loss time-scale due to a generic process, j, is usually defined from the emitted power as

$$\tau_{\mathrm{loss},j} = \left[\frac{1}{E}\left(\frac{\mathrm{d}E}{\mathrm{d}t}\right)_{\mathrm{loss},j}\right]^{-1}. \tag{A1}$$

The electron SYN time-scale is derived using the classical emitted power formula (see e.g. Rybicki & Lightman 1986; Longair 2011):

$$P_{\mathrm{syn}} \equiv \left(\frac{\mathrm{d}E}{\mathrm{d}t}\right)_{\mathrm{syn}} = \frac{4}{3}\sigma_T c \gamma^2 \beta^2 U_B. \tag{A2}$$

The IC emitted power is (see Jones 1968)

$$\left(\frac{\mathrm{d}E}{\mathrm{d}t}\right)_{\mathrm{IC}} = \frac{3\sigma_T c m_{\mathrm{e}}^2 c^4}{4}\int_0^\infty \mathrm{d}\epsilon\,\frac{n(\epsilon)}{\epsilon}\int_0^1 \mathrm{d}q\,\frac{\Gamma^2 q\, G(q,\Gamma)}{(1+\Gamma q)^3}, \tag{A3}$$

where the function $G(q, \Gamma)$ (which is part of the Klein–Nishina cross-section) is defined as

$$G(q,\Gamma) = 2q\log(q) + (1+2q)(1-q) + (\Gamma q)^2(1-q)/2(1+\Gamma q) \tag{A4}$$

with $\Gamma = 4\epsilon E_{\mathrm{e}}/m_{\mathrm{e}}^2 c^4$ and $q = E/\Gamma/(E_e - E)$. For the bremsstrahlung time-scale, we used (see e.g. Aharonian et al. 2013)

$$\tau_{\mathrm{brem}} \approx 4\times 10^7 \left(n/\mathrm{cm}^{-3}\right)^{-1}\ \mathrm{yr}, \tag{A5}$$

whereas the ionization time-scale for electrons is given by (see Schlickeiser 2002)

$$\tau_{\mathrm{ion}} \approx 1.9\times 10^9 \left(\frac{E}{100\,\mathrm{TeV}}\right)\left(\frac{n}{250\,\mathrm{cm}^{-3}}\right)^{-1}\ \mathrm{yr}, \tag{A6}$$

where we approximated the $\ln(\gamma)$ term to its value at 10 TeV as also done by Lacki & Thompson (2013).

Concerning protons, the time-scale for proton–proton inelastic scattering is given by

$$\tau_{\mathrm{pp}} = \left(n\sigma_{\mathrm{pp}}(E)c/\kappa\right)^{-1}, \tag{A7}$$

where κ is the inelasticity of the process and is $\kappa \approx 3K_\pi \approx 0.5$, where we used the value of K_π below equation (9). For the proton ionization energy loss, we use the following expression from

Schlickeiser (2002):

$$\left(\frac{\mathrm{d}E}{\mathrm{d}t}\right)_{\rm ion} \approx 1.82\times10^{-7}n \times [1+0.0185\ln(\beta)\,\Theta(\beta-0.01)] \times \frac{2\beta^2}{10^{-6}+2\beta^3}\ \mathrm{eV\,s^{-1}}, \quad \text{(A8)}$$

where $\beta = v/c$, and Θ is the step function. The Coulomb energy loss can be approximated by (see again Schlickeiser 2002)

$$\left(\frac{\mathrm{d}E}{\mathrm{d}t}\right)_{\rm Coul} \approx \frac{3.08\times10^{-7}n_{\rm e}\beta^2}{\beta^3+2.34\ 10^{-5}(T_{\rm e}/2.0\ 10^6K)^{1.5}} \times \Theta\left[\beta-7.4\times10^{-4}(T_{\rm e}/2.0\ 10^6K)^{1/2}\right]\ \mathrm{eV\,s^{-1}}, \quad \text{(A9)}$$

where and $T_{\rm e}$ and $n_{\rm e}$ are the plasma temperature and density, respectively.

APPENDIX B: PRODUCTION OF SECONDARY PARTICLES

For the sake of completeness, here we report the detailed formula used to calculate the production of secondaries as discussed in details in Kelner et al. (2006). In the following equations, we use the parameters $x \equiv E_j/E_\pi$ and $r \equiv 1-\lambda = (m_\mu/m_\pi)^2$, where the former is the fraction of energy of the lepton 'j' with respect the parent π meson, whereas the latter is the ratio between the muon and pion masses.

The muonic neutrinos produced in the direct process $\pi \longrightarrow \mu\nu_\mu$ is described by

$$f^{(1)}_{\nu_\mu}(x) = \frac{1}{\lambda}\,\delta(E_{\nu_{\rm e}}-E_{\nu_\mu})\,\theta[\lambda-x], \quad \text{(B1)}$$

while the electrons and muonic neutrinos produced by the muon decay $\mu \longrightarrow \nu_\mu\bar{\nu}_{\rm e}e$ are described by the following function:

$$f_{\rm e}(x) = f^{(2)}_{\nu_\mu}(x) = g_{\nu_\mu}(x)\,\theta[x-r] + \left[h^{(1)}_{\nu_\mu}(x)+h^{(2)}_{\nu_\mu}(x)\right]\theta[r-x], \quad \text{(B2)}$$

where the function g and h are defined as

$$g_{\nu_\mu}(x) = (9x^2-6\ln(x)-4x^3-5)(3-2r)/9/(1-r)^2,$$

$$h^{(1)}_{\nu_\mu}(x) = (9r^2-6\ln(r)-4r^3-5)(3-2r)/9/(1-r)^2,$$

$$h^{(2)}_{\nu_\mu}(x) = [9(r+x)-4(r^2+rx+x^2)](1+2r)(r-x)/(9r^2).$$

The electron neutrino function is

$$f_{\nu_{\rm e}}(x) = g_{\nu_{\rm e}}(x)\,\theta[x-r] + \left[h^{(1)}_{\nu_{\rm e}}(x)+h^{(2)}_{\nu_{\rm e}}(x)\right]\theta[r-x], \quad \text{(B3)}$$

where the functions g and h are defined as

$$g_{\nu_{\rm e}}(x) = \frac{2(1-x)\left[6(1-x)^2+r(5+5x-4x^2)+6r\ln(x)\right]}{3(1-r)^2},$$

$$h^{(1)}_{\nu_{\rm e}}(x) = \frac{2\left[(1-r)(6-7r+11r^2-4r^3+6r\ln(r)\right]}{3(1-r)^2},$$

$$h^{(2)}_{\nu_{\rm e}}(x) = \frac{2(r-x)\left(7r^2-4r^3+7xr-4xr^2-2x^2-4x^2r\right)}{3r^2}.$$

APPENDIX C: EBL APPROXIMATION

In this work, we use the EBL model developed in Franceschini & Rodighiero (2017) to account for $\gamma\gamma$ absorption during the propagation in the intergalactic medium. From a fitting procedure, we found the following analytic approximation that is able to reproduce their result for $z = 0.003$ with an accuracy $\lesssim$6 per cent. The approximate expression reads

$$\tau^*_{\gamma\gamma}(E) = \frac{95}{1100}\left\{\left[\frac{(E/1\,\mathrm{TeV})^{-2.7}}{2.1}+\frac{(E/1\,\mathrm{TeV})^{-0.31}}{0.34}\right]^{-1} + \left[\frac{(E/12\,\mathrm{TeV})^{-3.1}}{0.47}+\frac{(E/40\,\mathrm{TeV})^{-0.8}}{20}\right]^{-1} + 7\left(\frac{E}{100\,\mathrm{TeV}}\right)^{7.8}\right\}. \quad \text{(C1)}$$

We introduced the redshift dependence in our analytic formula of the optical depth as follows:

$$\tau_{\gamma\gamma}(E,z) = \tau^*_{\gamma\gamma}(E)\left[\frac{z}{0.003}\right], \quad \text{(C2)}$$

which has an accuracy $\lesssim$10 per cent when $z = 0.01$ and $\lesssim$20 per cent when $z = 0.03$.

APPENDIX D: ANALYTIC ESTIMATES FOR PRODUCTION OF SECONDARY AND TERTIARY ELECTRONS

In this Appendix, using simple analytical estimates, we show that secondary and tertiary electrons are always as important as primary ones if the SBN behaves approximately as a calorimeter for CR protons. We assumed throughout the paper that the injection spectrum of primary electrons is related to the protons one as $q_{\rm e} = q_{\rm p}(E)/50$. On the other hand, the injection of secondary electrons from pp scattering can be written as

$$q_{\rm pp\to e}(E) = n_{\rm ISM}\,\sigma_{\rm pp}\,c\,f_{\rm p}(E/\xi_{\rm e})/\xi_{\rm e}, \quad \text{(D1)}$$

where $\xi_{\rm e} \approx 0.05$ is the fraction of parent proton's energy transferred to the electron. The parent proton's spectrum is $f_{\rm p}(E) = q_{\rm p}(e)\tau_{\rm loss}(E)/\eta$, where the factor η accounts approximately for the transport condition: $\eta = 1$ for the calorimetric or 2 for the escape limited scenarios, respectively. Now, using $q_{\rm p}(E) \propto E^{-\alpha+2}$ and $\tau_{\rm loss} = (n_{\rm ISM}\sigma_{\rm pp}c)^{-1}$, and neglecting the mild energy dependence of $\sigma_{\rm pp}$, one easily found that

$$\frac{q_{\rm pp\to e}(E)}{q_{\rm e}(E)} \simeq \frac{50}{\eta}\xi^{\alpha-3} \approx 1, \quad \text{(D2)}$$

where we used $\alpha = 4.3$.

A similar result is valid for tertiary electrons produced from pair production. In this case, we can use the leading particle approach, where the energy of the photons is assumed to be transferred only to one of the two electrons. With this approach, we show that the ratio between tertiary and secondary electrons is approximately given by the $\gamma\gamma$ optical depth. The injection term for electron due to pair production reads

$$q_{\gamma\gamma\to{\rm e}}(E) = \int \mathrm{d}\epsilon\, n_{\rm bkg}(\epsilon)n_\gamma(E)\sigma_{\gamma\gamma}(E,\epsilon)\,c = n_\gamma(E)c\tau_{\gamma\gamma}(E)/R. \quad \text{(D3)}$$

Taking into account that the high-energy photon density can be approximated by the gamma-rays injected via the dominant π_0

decay mechanism, the following relation can be assumed:

$$n_\gamma(E) = \frac{R}{c} q_{\pi_0 \to 2\gamma}(E) = \frac{R}{c} n_{\rm ISM} \sigma_{\rm pp} f_{\rm p}(E/\xi_\gamma)/\xi_\gamma \,, \tag{D4}$$

where ξ_γ is the proton's energy transferred to the photon. Now, using equations (D3), (D4), and (D1) we can estimate the ratio between pair production and pp electrons as follows:

$$\frac{q_{\gamma\gamma \to {\rm e}}}{q_{\rm pp \to e}} \approx \frac{(R/c)\, n_{\rm ISM} \sigma_{\rm pp} f_{\rm p}(E/\xi_\gamma)/\xi_\gamma \, c\, \tau_{\gamma\gamma}/R}{n_{\rm ISM} \sigma_{\rm pp}\, c\, f_{\rm p}(E/\xi_{\rm e})/\xi_{\rm e}} = \tau_{\gamma\gamma}, \tag{D5}$$

where we assumed $\xi_{\rm e} \approx \xi_\gamma$. The later equality is valid only when $\tau_{\gamma\gamma} \leq 1$ then it saturates giving $q_{\gamma\gamma \to {\rm e}}/q_{\rm pp \to e} = 1$. Since the $\gamma\gamma$ optical depth can be roughly estimated using only the IR photon density, i.e.

$$\begin{aligned} \tau_{\gamma\gamma}(100\,{\rm TeV}) &\approx 0.2 \sigma_T \, R \, n_{\rm ph}(0.01\,{\rm eV}) \\ &\approx 4.123 \left(\frac{R}{100{\rm pc}}\right) \left(\frac{U_{\rm rad}}{10^3\,{\rm eVcm^{-3}}}\right) \\ &\times \left(\frac{\epsilon}{0.01\,{\rm eV}}\right)^{-1} \end{aligned} \tag{D6}$$

we observe that, for standard physical condition in a SBN, $\tau_{\gamma\gamma}$ easily reaches values larger than 1. Therefore, for a large energy range, one may expect that tertiary electrons are as important as secondary one.

A further channel for the production of secondary electrons is through the $p\gamma$ interaction. Nevertheless, the energy threshold of protons for such a process is $\sim 3 \times 10^{17}$ eV for protons interacting with 1 eV background photons and two orders of magnitude higher for the interaction with the FIR background. Considering that SBNi are probably incapable to accelerate protons up to such a very high energies, neglecting this term, as we did in this work, is widely justified.

This paper has been typeset from a TEX/LATEX file prepared by the author.